Materials Advances

ROYAL SOCIETY OF CHEMISTRY

PAPER

View Article Online
View Journal | View Issue

Cite this: *Mater. Adv.*, 2022, 3, 8771

Extended air, light, and heat-resistive organolead halide perovskite single-crystalline microrods for high-performance photodetectors†

Chang-Yu Lin, *[ab] Rajesh Kumar Ulaganathan, *[cde] Ambika Subramanian,[a] Huei-Chu Weng,[a] Yaw-Jen Chang,[a] Raghavan Chinnambedu Murugesan,[f] Raman Sankar [c] and Alex Rozhin[f]

Two-dimensional organic–inorganic hybrid perovskites are much attracted due to promising stable optoelectronic properties with tunable quantum well structures. Herein, we report the photodetector performance of the structurally tuned FA-incorporated hybrid perovskite FA-(N-MPDA)$PbBr_4$ (FA = formamidinium and N-MPDA = N^1-methylpropane-1,3-diammonium) high-quality single-crystalline microrods obtained from over supersaturated solution by a slow evaporation at constant temperature (SECT) growth method. The single crystalline FA-(N-MPDA)$PbBr_4$ microrod exhibits exceptional structural, thermal, and optical stabilities against ambient, light, and heat exposures, which were systematically monitored using X-ray diffraction, photoluminescence, and thermogravimetric analysis/differential scanning calorimetry techniques. The photodetector device fabricated using stable FA-(N-MPDA)$PbBr_4$ crystalline microrod exhibits good responsivity ~40 A W^{-1} with a response time of less than 50 ms by shining a 405 nm laser. In addition, the microrods exhibit high specific detectivity of 7.8×10^{10} Jones at an incident light of 53 μW cm^{-2}. These results demonstrate the potential of organic–inorganic perovskite microrods formed with a long-chain organic diammonium spacer suitable for stable and high-performance optoelectronic devices.

Received 28th May 2022,
Accepted 15th September 2022

DOI: 10.1039/d2ma00602b

rsc.li/materials-advances

1. Introduction

Three-dimensional (3D) organometal halide ABX_3 perovskites, A = methyl ammonium $CH_3NH_3^+$ (MA)/or formamidinium (FA) $HC(=NH)NH_3^+$ cations, B = Pb^{2+}/Sn^{2+}, and X = Cl^-, Br^-, and I^- are widely explored for optoelectronic applications such as photodetectors,[1] field-effect transistors,[2] solar cells,[3] and random lasers.[4–6] However, this class of materials often suffers degradation due to poor stability against light, moisture, and heat atmosphere.[7,8] Two-dimensional (2D) layered perovskites have recently gained much attention because of their stability and inherent quantum well (QW) structures.[9–11] The 2D perovskites consist of an inorganic and organic portion, while inorganic perovskite slabs, which are sandwiched between the organic barrier layers to form a QW assembly, form the 2D conducting layers. There is a dielectric constant difference between the organic and inorganic structure, which creates the efficient confinement of electron–hole pairs in the 2D perovskite system. Consequently, this induces a stable structure in the ambient environment.[12–14]

Compared to 3D hybrid halide perovskites, 2D materials offer significant advantages in tuning the physical properties by tailoring the crystal structure using different organic spacers, varying perovskite layer thickness, and halide ion modifications.[15,16] Based on the crystallographic studies, layered inorganic perovskite sheets are typically formed by slicing 3D perovskites using the (001) or (110) planes. There are many reports on the 2D hybrid perovskites with different organic spacers, metal ions, and halides.[17,18] Recently, alkyl diammonium cations having different carbon chain lengths, such as N^1-methylethane-1,3-diammonium (NMEDA) and N^1-methylpropane-1,3-diammonium (NMPDA), were used as organic spacers to form the self-assembly of (110)- and (001)-oriented (N-MEDA)$PbBr_4$ (corrugated crystal structure) and

[a] *Department of Mechanical Engineering, Chung Yuan Christian University, Taoyuan-32023, Taiwan. E-mail: cylin@cycu.edu.tw*
[b] *Research Center for Semiconductor Materials and Advanced Optics, Chung Yuan Christian University, Taoyuan-32023, Taiwan*
[c] *Institute of Physics, Academia Sinica, Taipei-11529, Taiwan*
[d] *Center for Condensed Matter Sciences, National Taiwan University, Taipei-10617, Taiwan*
[e] *Department of Electrical and Photonics Engineering, Technical University of Denmark, Roskilde-4000, Denmark. E-mail: rajul@fotonik.dtu.dk*
[f] *Aston Institute of Photonic Technologies, Aston University, Birmingham-B4 7ET, UK*

† Electronic supplementary information (ESI) available. See DOI: https://doi.org/10.1039/d2ma00602b

(N-MEDA)$PbBr_4$ perovskites, respectively. The 2D (N-MEDA)-$PbBr_4$ perovskite exhibits a strong, broadband white light emission, whereas (N-MPDA)$PbBr_4$-based 2D hybrid perovskite exhibits a strong excitonic absorption band at 420 nm (blue region). The growth of a high-quality single crystal of this material is essential for the fundamental understanding and application points of view.

Moreover, hybrid perovskites in the single crystal form exhibit long carrier diffusion, high absorption, enhanced charge transport due to large grain boundaries, and low defect concentration.[19–21] We have recently reported unprecedented random lasing from FA-incorporated FA-(NMPDA)$PbBr_4$ single-crystalline rods grown by the SECT growth method as the optical gain media. The millimeter-sized single-crystalline FA-(NMPDA)$PbBr_4$ microrods reveal low threshold ($\sim$0.5 μJ cm^{-2}) random lasing behaviors with a sharp laser having linewidth ($\sim$0.1 nm) and a high-quality factor ($\sim$5350) at room temperature.[22] The FA was incorporated into the 2D perovskite lattice to form the quasi-2D perovskite-like structure and enhance the stability. The FA-(NMPDA)$PbBr_4$ single-crystalline microrods showed excellent stability for more than 2 hours against laser irradiation.[22]

Motivated by the outstanding stability against laser irradiation of the single-crystalline FA-(NMPDA)$PbBr_4$ microrods, in this study, we have further extended its application as a single crystalline microrod conductive channel material in the photodetector device structure. Furthermore, the single crystalline microrods were subjected to essential characterization to evaluate the quality and structure–property relations. The FA-(N-MPDA)$PbBr_4$ microrods exhibit high photoresponsivity of $\sim$40 A W^{-1} (under 405 nm laser illumination) and high specific directivity with robust photoswitching stability under continuous laser irradiations with a fast response speed. These results demonstrate that the FA-(N-MPDA)$PbBr_4$ microrod holds great promise for optoelectronic applications, exclusively for constructing photodetectors with great photocurrent generation, fast response, and long-term stability.

2. Results and discussion

Fig. 1a illustrates the SECT process for the growth of millimeter-sized perovskite single-crystalline microrods. At first, the as-synthesized FA-(N-MPDA)$PbBr_4$ compound (Fig. S1, ESI†) was saturated by dissolving into HBr solvent at 110 °C under continuous magnetic stirring. The solution was subjected to constant magnetic stirring to form a clear solution without undissolved debrides. The homogeneous saturated solution obtained by the above process allowed the slow evaporation at a constant temperature for supersaturation. During the nucleation, the excessive solute in the supersaturated solution crystallizes at the bottom of the beaker. Further, the solution was left for continuous slow evaporation for 2–3 days at a constant temperature without any disturbance to achieve high-quality single-crystalline, a millimeter-sized microrod. The optical image of the as-synthesized transparent yellowish single-crystalline FA-(N-MPDA)$PbBr_4$ microrod is shown in Fig. 1b. The size of the as-grown microrod is 3 mm in length and 2 μm in diameter. The inset in Fig. 1b is the scanning electron microscopy (SEM) image of the as-grown

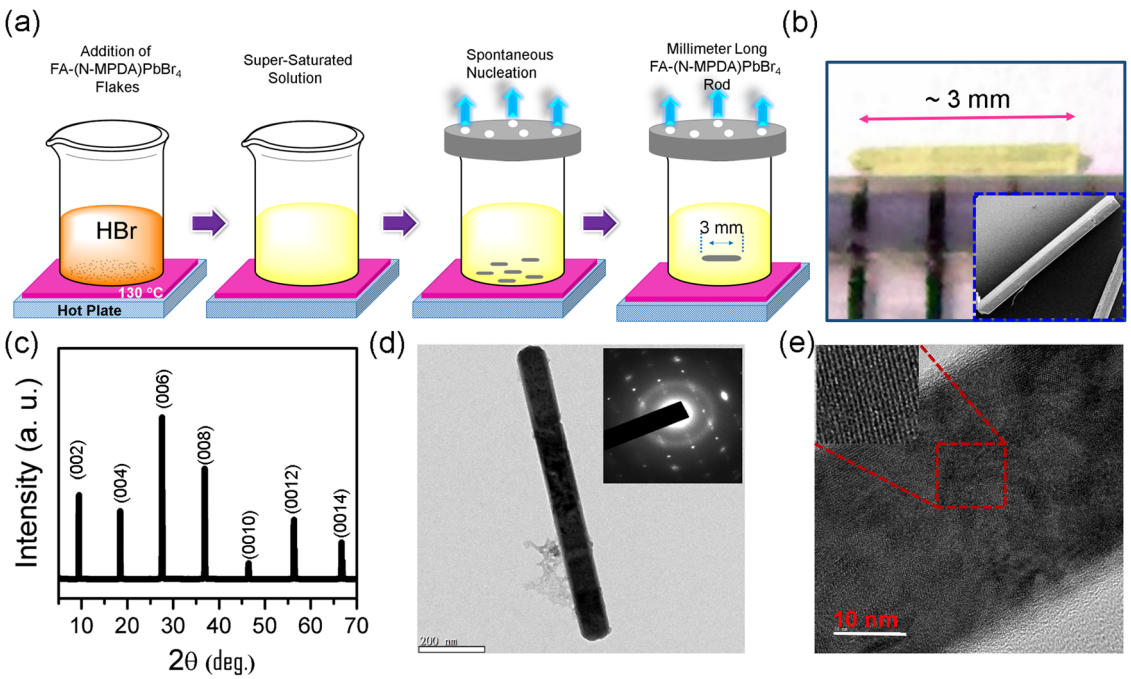

Fig. 1 (a) Diagrammatic sketch of the single crystal growth of the FA-(N-MPDA)$PbBr_4$ microrod. (b) Optical image of the as-grown microrod with a length of $\sim$3 mm in size. The inset displays the SEM image of the FA-(N-MPDA)$PbBr_4$ microrod with higher magnification. (c) XRD *hkl* planes of the FA-(N-MPDA)$PbBr_4$ microrod. (d) TEM image and its corresponding SAED pattern. (e) FA-(N-MPDA)$PbBr_4$ microrod lattice fringes are revealed with the HRTEM image and found to be $\sim$0.25 nm.

millimeter-sized perovskite microrod having a smooth surface. The XRD pattern shown in Fig. 1c confirms the solid diffraction peaks consistent with interplanar spacing at 2θ values of 9.08°, 18.18°, 27.25°, 36.63°, and 46.20°, which correspond to the lattice planes of (002), (004), (006), (008), and (0010), respectively.[22] From the single crystal XRD study, the single crystalline microrod exhibits a monoclinic crystal structure, and the growth direction is oriented along the *c*-axis. The lattice parameter values are identified as a = 12.83, b = 5.94, and c = 13.17 with the space group of $P2/m$. A transmission electron microscopy (TEM) study was carried out to reveal the single crystallinity of the FA-(N-MPDA)$PbBr_4$ microrod, as shown in Fig. 1d. The single crystalline surface of the perovskite microrod is very smooth. It has no surface damage due to the incident electron beam. The inset Fig. 1d shows the selected area electron diffraction (SAED) pattern with linearly ordered diffraction spots, which indicates the single-crystalline nature of the FA-(N-MPDA)$PbBr_4$ microrod. The careful observation of the SAED pattern reveals the dual/multi-sports features, indicating the stacking fault in the atomic arrangement in the perovskite lattices. The lattice fringes were observed from the high-resolution transmission electron microscopy (Fig. 1e), and the interplanar distance was found to be ~0.25 nm. Moreover, the stacking fault and break in lattice arrangement are revealed in the high-resolution TEM pattern, which correlates well with the SAED result. The formation of stacking fault and unparalleled fringes in the SAED (inset of Fig. 1d) and HRTEM (inset of Fig. 1e) might be attributed to the FA cation in the crystal structure.

To assess the chemical uniformity, the as-grown FA-(N-MPDA)-$PbBr_4$ microrod crystal was further examined by energy-dispersive X-ray (EDX) spectroscopy. EDX mapping (Fig. 2a) confirms the uniformly distributed C, N, Pb, and Br atoms in the single-crystalline microrod. The EDX spectrum of the FA-(N-MPDA)-$PbBr_4$ microrod is displayed in Fig. S2 of the ESI,† which shows the prominent individual peaks of all the atoms such as Pb, Br, N, and C. Further, to study the optical properties and spectral uniformity of the as-grown FA-(N-MPDA)$PbBr_4$ microrod single crystals, we performed photoluminescence (PL) spectral analysis. The microrods were placed on a clean silicon substrate and excited by a 405 nm laser using a 10× objective with a light intensity of 1 mW. Fig. 2b is the PL emission spectrum of the FA-(N-MPDA)$PbBr_4$ microrod with a narrow emission band at a wavelength of 535 nm. The PL emission for the pristine (NMPDA)$PbBr_4$ without FA was observed at the blue band region of wavelength of about 435 nm (Fig. S3, ESI†). The PL emission at the green band region for the FA-(N-MPDA)$PbBr_4$ is well correlated to the change in the crystal structure compared to the pristine (NMPDA)$PbBr_4$. To ensure the spectral uniformity of the microrod, spatially-correlated PL mapping was performed. Fig. 2c shows the microrod optical mapping image (in Fig. S4, ESI†), and the distribution PL emission mapping is shown in Fig. 2d, recorded with 64 × 64 pixels. The distribution of the PL emission peaks was visualized over the entire crystal through spectral mapping, endorsing the reasonable quality of the FA-(N-MPDA)$PbBr_4$ microrods. Finally, the histogram of the whole mapping area was calculated. The peak distribution was identified between 526 nm and 545 nm (inset Fig. 2d). The absorption spectrum of the FA-(N-MPDA)$PbBr_4$ microrods was observed in the 400–800 nm wavelength region, which shows strong absorption (Fig. S5, ESI†).

The structural, optical, and thermal stability of the FA-(N-MPDA)$PbBr_4$ microrod exposed under ambient atmosphere (room temperature 30 °C and humidity 70%) were systematically

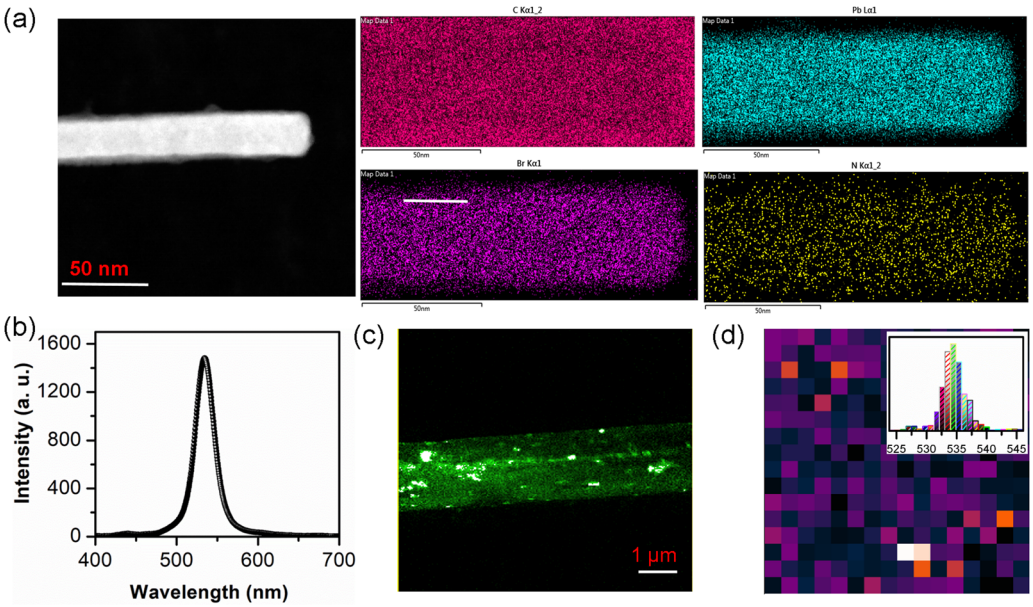

Fig. 2 (a) Elemental mapping of the microrod was analyzed, and all elements were distributed uniformly. (b) The emission peak of the as-synthesized FA-(N-MPDA)$PbBr_4$ is observed at 535 nm. (c) Optical mapping image of the FA-(N-MPDA)$PbBr_4$ microrod. (d) Peak spectral mapping of a microrod confirms the spectral uniformity of the crystal growth. At the inset, the corresponding histogram distribution of the wavelength is displayed; the maximum emission center percentage is obtained at 535 nm.

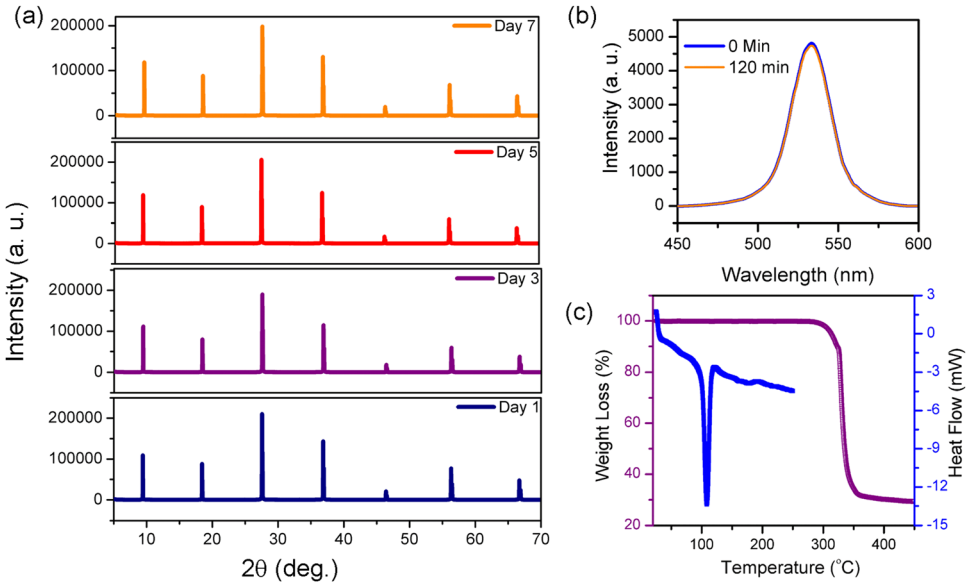

Fig. 3 (a) XRD patterns of the FA-(N-MPDA)$PbBr_4$ microrod for 1, 3, 5, and 7 days. (b) The FA-(N-MPDA)$PbBr_4$ microrod crystal shows stable PL emission without any degradation and damage even after 120 min of continuous exposure to laser and ambient environment. (c) Weight loss percentile curve of the FA-(N-MPDA)$PbBr_4$ powder under various temperatures.

monitored using XRD, PL, and TGA/DSC, and the results are summarized in Fig. 3. The XRD measurement was conducted from days 1 to 7 (Fig. 3a), revealing no changes in the XRD patterns. The peak positions and intensities of the FA-(N-MPDA)$PbBr_4$ crystalline microrod remain almost the same as it was observed freshly, and there are no additional peaks corresponding to the impurity/secondary phases, which confirms the exceptional structural stability and crystallinity against ambient degradation.

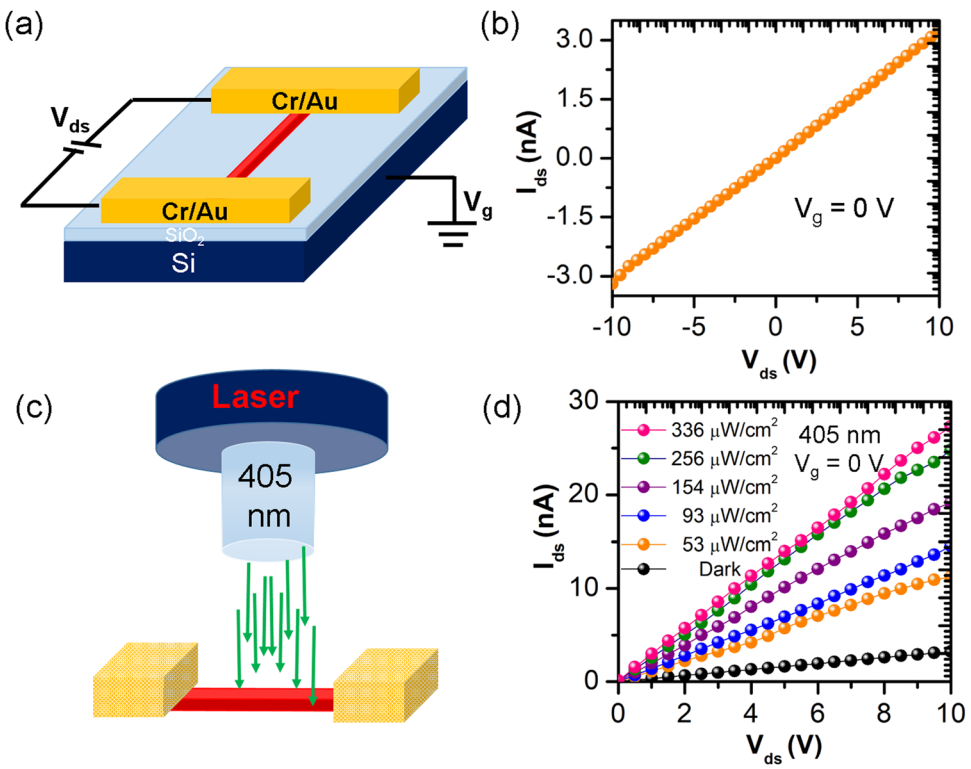

Fig. 4 (a) The schematic illustration of a FA-(N-MPDA)$PbBr_4$ microrod-FET. (b) The output characteristic curve of I_{ds} *vs.* V_{ds} obtained at V_g is at 0 V. (c) The optoelectronic investigation was conducted by illumining the FA-(N-MPDA)$PbBr_4$ microrod with a 405 nm laser. (d) Typical output curves of a FA-(N-MPDA)$PbBr_4$ microrod photodetector attained in the dark and with the lighting of various intensities (53, 93, 154, 256, and 336 μW cm^{-2}) at V_g = 0 V.

Fig. 3b shows the PL emission spectrum of the FA-(N-MPDA)$PbBr_4$ microrod under continuous laser irradiation of 405 nm. The PL intensity of the emission spectrum remains the same even after continuous laser light irradiation for about two hours. The results above prove that the FA-(N-MPDA)$PbBr_4$ microrod is stable against light and ambient exposure. To evaluate the thermal stability, chemical decomposition, and phase transition behavior of the material, TGA/DSC measurement was performed on the FA-(N-MPDA)$PbBr_4$ powder sample, as shown in Fig. 3c. The FA-(N-MPDA)$PbBr_4$ exhibits stable weight until 290 °C without any loss of chemical decomposition, indicating the heat resistance of the material until 290 °C, which is 50 °C and 100 °C higher than that of the 2D$(PEA)_2PbBr_4$ and $(BA)_2PbI_4$ hybrid perovskite materials, respectively.[23,24] After 290 °C, the material drops to about 70% of its original weight before reaching 350 °C due to the loss of organic moieties, such as the decomposition of FA and N-MPDA species.[25] The formation of a sharp endothermic peak at 110 °C was observed from the differential scanning calorimetric analysis (Fig. 3c), indicating the structural phase transition of the material.

Moreover, the phase transition of the material occurred before the decomposition temperature, as observed in the TGA result. The superior stability of the FA-(N-MPDA)$PbBr_4$ perovskite crystalline microrod can be reasoned to form a stable perovskite crystal structure due to the high tolerance factor of the organic species (FA and long-chain diammonium N-MPDA spacer) and Br^- ion in the perovskite lattices.[26,27] Moreover, the higher lattice energy was caused by a smaller Pb–Br bond length in the perovskite lattices avoiding materials decomposition, which quickly occurred in iodide-based perovskites due to low lattice energy.[26] In overall consideration, the FA-(N-MPDA)$PbBr_4$ crystalline microrod possesses excellent stability against heat, light, and moisture, which typically appears to be a critical challenge in other 3D and 2D hybrid halide perovskites for implementing this material into practical applications.

A photodetector device was made on the as-grown FA-(N-MPDA)$PbBr_4$ microrod single crystal to evaluate the optoelectronic performances by depositing source–drain electrodes (Cr/Au). This was achieved using a copper grid as a shadow mask on both ends of the FA-(N-MPDA)$PbBr_4$ perovskite microrod, and the entire device structure is on a silicon substrate having a 300 nm dielectric layer.[28,29] The schematic view of the device structure is shown in Fig. 4a. The source–drain voltage *vs.* source–drain current (I_{ds}–V_{ds}) characteristic of the FA-(N-MPDA)$PbBr_4$ microrod was measured under dark between −10 and 10 V at V_g = 0 V in the atmospheric environment (Fig. 4b). Fig. S6 of the ESI,† shows linear I_{ds}–V_{ds} behavior at a lower voltage of −0.5 to 0.5 V, confirming the Ohmic contact between the metal pad and perovskite microrod. The schematic

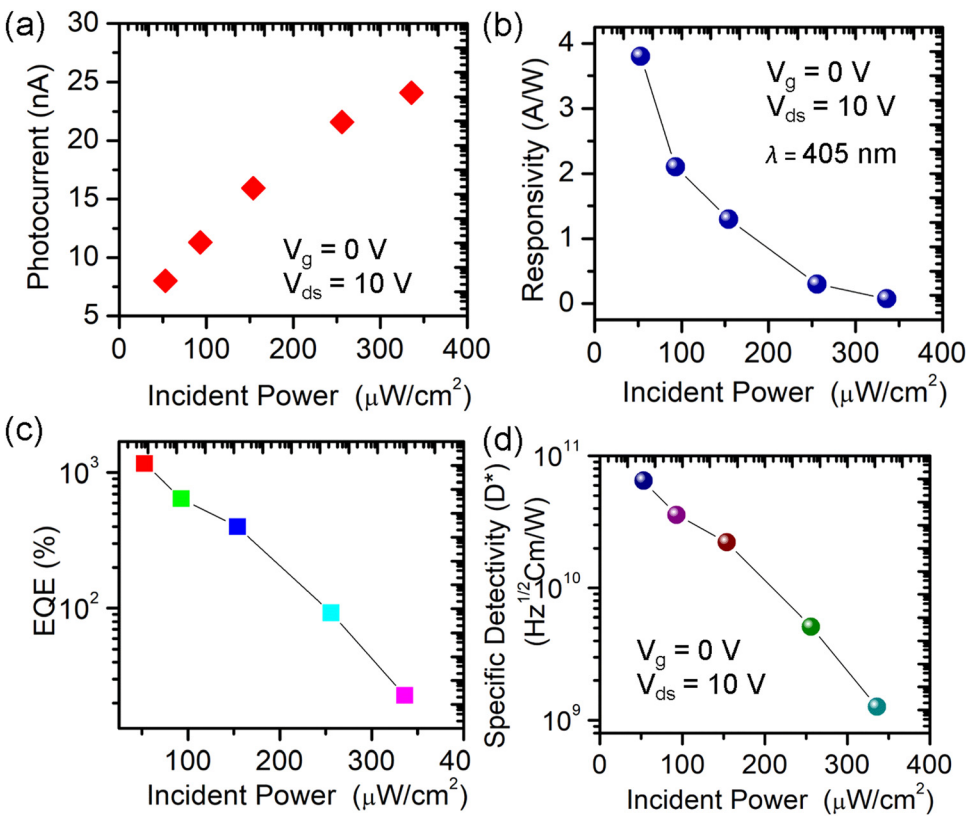

Fig. 5 (a) Photocurrent as a function of incident power at V_{ds} = 10 V and V_g = 0 V. (b) Photoresponsivity of the FA-(N-MPDA)$PbBr_4$ microrod under different laser intensities at 405 nm. The FA-(N-MPDA)$PbBr_4$ microrod photodetector shows a maximal R_λ of 3.8 A W^{-1} excited at 53 μW cm^{-2}, V_g = 0 V, and V_{ds} = 10 V. (c and d) The calculated laser power dependencies of EQE and D^* for the FA-(N-MPDA)$PbBr_4$ microrod at V_g = 0 V and V_{ds} = 10 V.

illustration of the photoresponse of the FA-(N-MPDA)$PbBr_4$ microrod under a 405 nm laser illumination is depicted in Fig. 4c.

Fig. 4d shows the plot of the generated photocurrent (I_{ph}) as a function of various light intensities. The photocurrent increased with increasing laser intensity (53 to 336 μW cm^{-2}) as well as with the bias voltage (0 to 10 V) compared to the dark measurement (Fig. 4d). The I_{ph} value was obtained by subtracting the dark current (I_{dark}) from the light current (I_{light}). At the illumination of 336 μW cm^{-2} and a bias of 10 V, the device attained a high photocurrent of 24 nA (Fig. 5a). The photocurrent *vs.* bias voltage is shown in Fig. S7 of the ESI.† From Fig. S7, the photocurrent increases with an increase in the bias voltage. The photoresponsivity (R_λ) of the FA-(N-MPDA)$PbBr_4$ microrod photodetector is estimated using $R_\lambda = I_{ph}/(P \times S)$, where I_{ph} is the photocurrent, P is light irradiance, and S is the active area of the device.[30,31] From the above relation, the photoresponsivity of the FA-(N-MPDA)$PbBr_4$ microrod is ~3.8 A W^{-1} (Fig. 5b) under a light illumination of 53 μW cm^{-2} (V_g = 0 V and V_{ds} = 10 V). Photoresponsivity is considered to be a critical figure of merit of the photodetector.[32–36] The high photoresponsivity value on the perovskite microrod was attributed to the strong absorption coefficient, unidirectional charge transport, high-quality factor, quantum confinements, and low non-radiative recombination rates.

The other two key factors of photosensing are external quantum efficiency (EQE) and specific detectivity (D^*). EQE defines photoexcited electrons produced per incident photons and is expressed as EQE = $R_\lambda \cdot [hc/(e\lambda)]$, where R_λ is the photoresponsivity, h is Planck's constant, c is the speed of light, e is the elementary charge, and λ is the incident light wavelength.[37,38] From Fig. 5c, the estimated EQE for the FA-(N-MPDA)$PbBr_4$ single-crystalline microrod is ~10^3. The obtained high value of EQE can be related to the prolonged lifetime of the photoexcited charge carriers, which transit the device several times, enhance the efficiency, and recombine. The other parameter (D^*) defines the photodetector sensitivity by detecting the minimum light optical signals. It is calculated by $D^* = (S \cdot \Delta f)^{1/2}/\mathrm{NEP}$, where S is the effective area, Δf is the electrical bandwidth, and NEP is the noise equivalent power. The above relation is rewritten as $R_\lambda S^{1/2}/(2eI_{dark})^{1/2}$ at a lower NEP value, where R_λ, S, e, and I_{dark} are the photoresponsivity, effective area, elementary charge, and dark current, respectively.[39,40] The calculated D^* value is 7.8×10^{10} Jones (Fig. 5d) at 53 μW cm^{-2} (V_g = 0 V and V_{ds} = 10 V).

Fig. 6a illustrates the I_{ds} curve of the FA-(N-MPDA)$PbBr_4$ microrod at different gate voltage ranging from −20 V to 50 V under dark and laser irradiation conditions. At 140 mW of 405 nm illumination, the I_{ds} current undoubtedly enhances than that in the dark. At positive V_g, the current increases, depicting the n-type nature of the material with more electrons as a charge carrier. The I_{ph} is extracted and plotted against V_g from the transfer curve (Fig. 6a), as shown in the ESI,† in

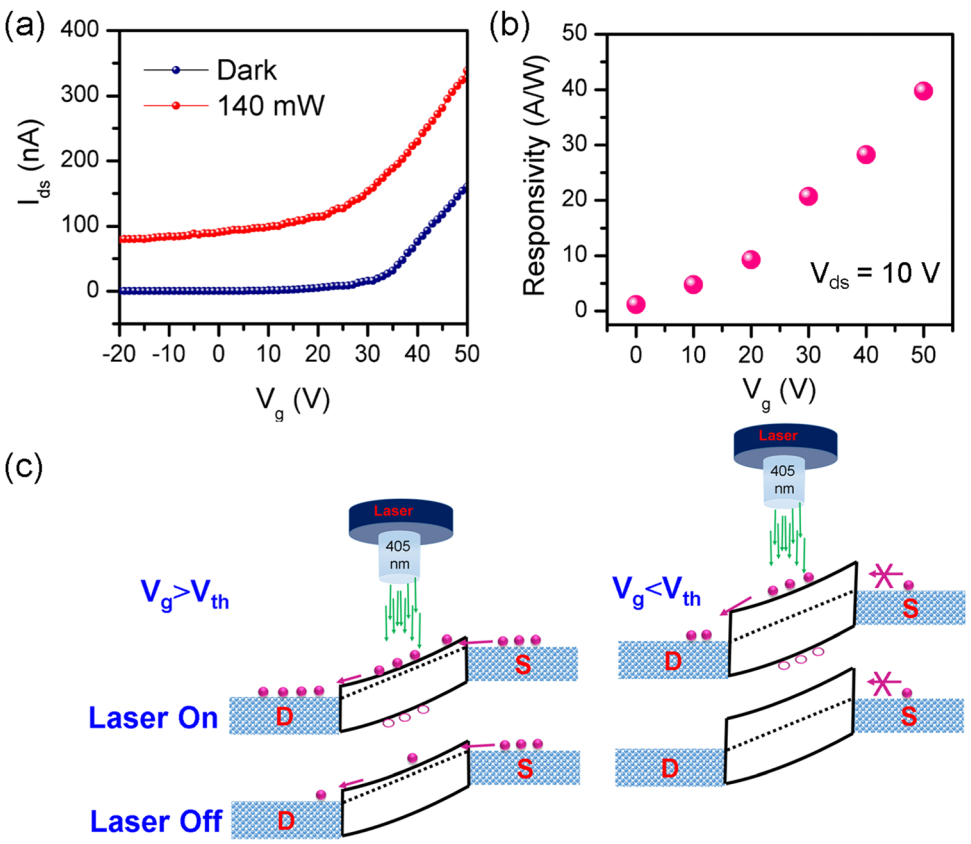

Fig. 6 (a) The FA-(N-MPDA)$PbBr_4$ microrod transfer curve under the illuminated and dark states. (b) R_λ at 140 mW of 405 nm under various V_g from 0 to +50 V at V_{ds} = 10 V. (c) Band diagram at laser On and Off conditions with higher and lower threshold voltages.

Fig. S8. The R_λ is calculated concerning various V_g (0 to 50 V) at 10 V of V_{ds} shown in Fig. 6b. The R_λ increases when V_g rises and gives a maximum R_λ of 40 A W^{-1} at 50 V. The mechanism behind this high value of R_λ is demonstrated in Fig. 6c. In (Laser Off) condition at $V_g > V_{th}$, the I_{ds} continually increases when the V_g is more than the threshold voltage (V_{th}) due to the Fermi level band shifting upward, thus allowing more charge carrier flows into the source–drain electrodes. In the case of $V_g < V_{th}$, the I_{ds} value is much lower because the Fermi level shifts to a more downward direction, which creates a solid barrier for the circulation of charge carriers during electric field supply. During Laser On at $V_g > V_{th}$, the photons constantly produce numerous electron–hole pairs with less barrier for the circulation of carriers; both cause a much larger source–drain current, resulting in significant photocurrent enhancement, while at $V_g < V_{th}$, only a few exciting carriers will attain a chance to transit toward the electrode due to its long barrier.[41,42]

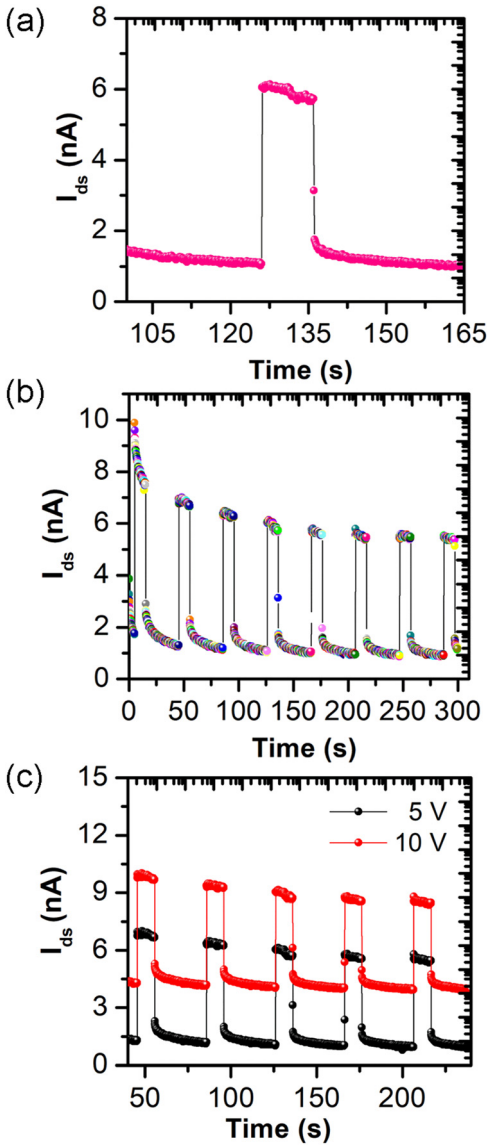

Fig. 7 (a) Real-time photoresponse of the FA-(N-MPDA)$PbBr_4$ microrod photodetector was measured at P = 93 μW cm^{-2} (λ = 405 nm), V_g = 0 V, and V_{ds} = 10 V under an on-off laser; from the single-cycle, the response speed is found to be less than 50 ms. (b) Photoswitching stability of a FA-(N-MPDA)$PbBr_4$ microrod in response to a train of pulsed illumination. (c) Time-resolved photoresponse of the FA-(N-MPDA)$PbBr_4$ photodetector was examined at different V_{ds}.

Typically, the presence of a long chain organic spacer in the hybrid perovskite impacts the conductivity, prohibiting the charge carrier transport process along its orientation, which might be attributed to the low conductivity of the FA-(N-MPDA)$PbBr_4$ microrod. The less conductance leads to low current (~3 nA) during bias between the source and drain. However, superior stability was observed from the microrod device under ambient air for several days. The long-term stability of the photodetector device was monitored on different days, as shown in the ESI,† in Fig. S9. The device exhibited good stability under ambient air for several days. Moreover, the PD device also reveals good thermal stability and increasing source–drain current until about 100 °C, as shown in Fig. S10 (ESI†). Later, the source–drain value decreased above 100 °C, indicating the degradation of organic molecules in the FA-(N-MPDA)$PbBr_4$ at higher temperatures.

Finally, real-time measurements were performed to show the response speed and photoswitching stability of the FA-(N-MPDA)$PbBr_4$ microrod photodetector with laser on-off illumination. Fig. 7a shows the single on-off cycle response, where a fast rise in the current (I_{ds}) under "on" and a quick drop after switching "off" the laser illumination are observed. The photocurrent increases rapidly, then decreases rapidly until it reaches a saturation level. This slight instability might be attributed to the presence of defects and surface oxygen, resulting in the generation and recombination of charge carriers, which significantly impact the capacity of generating and storing charges during the processes of photoresponse. In addition, the microrod defects or light/bias-induced degradation could also impact this instability of the photocurve. The photogenerated signal determined that the rising time of the FA-(N-MPDA)$PbBr_4$ microrod device is less than 50 ms. In the case of falling, there is a combination of fast decay and slow relaxation. To understand the successive photoswitching, the robustness and stability of the FA-(N-MPDA)$PbBr_4$ microrod photodetector were further inspected by a train of pulsed illumination for a long run-up to five-minute (Fig. 7b) and with various V_{ds} of 5 V and 10 V, where the I_{ds} increased when V_{ds} is higher (Fig. 7c). The reproducible on-off cycle without any degradation against laser illumination and atmospheric environment, along with maintainable rise times, reveals the device robustness, reproducible response, and switching stability of the FA-(N-MPDA)$PbBr_4$ microrod photodetector.[43,44]

3. Conclusion

In summary, the millimeter-sized FA-(N-MPDA)$PbBr_4$ perovskite single-crystalline microrod was grown by the SECT solution growth method for photodetector application. The FA-(N-MPDA)-$PbBr_4$ exhibits exceptional structural, optical, and thermal

stability against ambient, light, and heat, resulting in high-performance stable photodetectors. The FA-(N-MPDA)$PbBr_4$ single-crystalline microrod photodetector reveals stable photoresponse with a responsivity of $\sim$40 A W^{-1} and a specific detectivity of 7.8×10^{10} Jones at room temperature. Moreover, the device shows a fast response speed of less than 50 ms with robust photoswitching stability. High stability against natural degradation and good optoelectronic performance of the FA-(N-MPDA)$PbBr_4$ microrod would be a highly competitive perovskite material for implementing practical applications.

4. Experimental section

4.1. Precursor material for the single-crystal growth of (N-MPDA)$PbBr_4$

Lead oxide (PbO), hydrobromic acid (HBr), N^1-methylpropane-1,3-diammonium ($CH_3NH(CH_2)_3NH_2$) (N-MPDA), and formamidinium chloride ($HC(NH_2)_2Cl$) raw chemicals were purchased from Sigma Aldrich. 10 mmol PbO was dissolved in 20 mL HBr at 70 °C under constant stirring until a clear, bright yellow solution (Solution A) formed. On the other side, 3.33 mmol $CH_3NH(CH_2)_3NH_2$ was added dropwise into the HBr solution under ice bath conditions to prepare (N-MPDA)$^+Br^-$ salt solution (Solution B). To attain the 2D (N-MPDA)$PbBr_4$ perovskite, the cold salt solution B was added to hot solution A at 120 °C. Initially, light yellow precipitation will occur, redissolved with excessive HBr, and stirred to obtain a bright yellow solution.[22] This bright yellow solution is kept constant under slow evaporation[22,44,45] at a fixed temperature to obtain the (N-MPDA)$PbBr_4$ perovskite compound.

4.2. Formation of the FA-(N-MPDA)$PbBr_4$ perovskite

Formamidinium chloride (FACl) was added into the PbO solution first, followed by the addition of (N-MPDA)$^+Br^-$ with continued stirring. Following SECT growth techniques, the supersaturated solution evaporates slowly for 2–3 days while maintaining a constant temperature.[44,45] In nucleation, the excess solute in the supersaturated solution crystallizes at the bottom of the solution in millimeter sizes.

4.3. Characterization

The crystal structure and phase purity of the as-grown FA-(N-MPDA)$PbBr_4$ single crystal were examined with an X'Pert PRO-PANalytical XRD using CuKα (λ = 1.5406 Å) source, step size 0.01°, scan speed 0.5 s $step^{-1}$, and operation voltage 40 kV. SEM (FEI, Nova 200) investigated the morphology and elemental compositions. TEM (JEOL, JEM-2100F) was employed at 200 kV to study the microstructures and SAED patterns. TGA/DSC was performed on the powdered samples to observe the thermal stability using Mettler Toledo. The samples were taken in alumina crucibles and heated up to 450 °C at a 10 °C min^{-1} rate under an argon gas flow. A home-built setup was used to map under a 450 nm pulse laser (Pico Quant). The electrical and optical properties were measured at room temperature using (Lakeshore, TTPX) probe station. The system was combined with a source meter (Keithley, 2636A) with the optical system of a 405 nm laser.

4.4. Device fabrication

FA-(N-MPDA)$PbBr_4$ microrod-FETs were fabricated using a standard shadow mask technique with a copper grid. Gold/Chromium electrodes were deposited at about 100/10 nm on both ends of the microrods with the help of a thermal evaporator to attain the source and drain electrodes.[28,29] The effective illuminated area of the device was about 150 μm^2.

Conflicts of interest

There are no conflicts to declare.

Acknowledgements

C.-Y. L. acknowledges the financial support provided by the National Science and Technology Council (NSTC), Taiwan, under grant numbers NSTC-111-2112-M-033-005-, NSTC-110-2221-E-033-022, and NSTC-111-2628-E-033-002-MY3. R. S. acknowledges MOST-111-2124-M-001-009, MOST-110-2112-M-001-065-MY3, and Academia Sinica for the budget of AS-iMATE-19-112. R. C. M. and A. R. acknowledge the Marie Skłodowska-Curie Individual Fellowship (MOFUS, #795356).

References

1 R. Dong, Y. Fang, J. Chae, J. Dai, Z. Xiao, Q. Dong, Y. Yuan, A. Centrone, X. C. Zeng and J. Huang, *Adv. Mater.*, 2015, **27**, 1912.
2 S. Shao, W. Talsma, M. Pitaro, J. Dong, S. Kahmann, A. J. Rommens, G. Portale and M. A. Loi, *Adv. Funct. Mater.*, 2021, **31**, 2008478.
3 Y. Jiang, E. J. J.-Perez, Q. Ge, S. Wang, M. R. Leyden, L. K. Ono, S. R. Raga, J. Hu and Y. Qi, *Mater. Horiz.*, 2016, **3**, 548.
4 A. Zhizhchenko, S. Syubaev, A. Berestennikov, A. V. Yulin, A. Porfirev, A. Pushkarev, I. Shishkin, K. Golokhvast, A. A. Bogdanov, A. A. Zakhidov, A. A. Kuchmizhak, Y. S. Kivshar and S. V. Makarov, *ACS Nano*, 2019, **13**, 4140.
5 A. Kojima, K. Teshima, Y. Shirai and T. Miyasaka, *J. Am. Chem. Soc.*, 2009, **131**, 6050.
6 S. Huang, P. Huang, L. Wang, J. Han, Y. Chen and H. Zhong, *Adv. Mater.*, 2019, **31**, 1903830.
7 Y. Zhou and Y. Zhao, *Energy Environ. Sci.*, 2019, **12**, 1495.
8 J. Bisquert and E. J. J.-Perez, *J. Phys. Chem. Lett.*, 2019, **10**, 5889.
9 F. A. Roghabadi, M. Alidaei, S. M. Mousavi, T. Ashjari, A. S. Tehrani, V. Ahmadi and S. M. Sadrameli, *J. Mater. Chem. A*, 2019, **7**, 5898.
10 M. You, H. Wang, F. Cao, C. Zhang, T. Zhang, L. Kong, L. Wang, D. Zhao, J. Zhang and X. Yang, *ACS Appl. Mater. Interfaces*, 2020, **12**, 43018.

11 H. Yu, Y. Xie, J. Zhang, J. Duan, X. Chen, Y. Liang, K. Wang and L. Xu, *Adv. Sci.*, 2021, **8**, 2004510.
12 X. Zhang, X. Ren, B. Liu, R. Munir, X. Zhu, D. Yang, J. Li, Y. Liu, D.-M. Smilgies, R. Li, Z. Yang, T. Niu, X. Wang, A. Amassian, K. Zhao and S. Liu, *Energy Environ. Sci.*, 2017, **10**, 2095.
13 Y. Chen, Y. Sun, J. Peng, W. Zhang, X. Su, K. Zheng, T. Pullerits and Z. Liang, *Adv. Energy Mater.*, 2017, **7**, 1700162.
14 Z. Li, N. Liu, K. Meng, Z. Liu, Y. Hu, Q. Xu, X. Wang, S. Li, L. Cheng and G. Chen, *Nano Lett.*, 2019, **19**, 5237.
15 C. C. Stoumpos, D. H. Cao, D. J. Clark, J. Young, J. M. Rondinelli, J. I. Jang, J. T. Hupp and M. G. Kanatzidis, *Chem. Mater.*, 2016, **28**, 2852.
16 C. Liang, H. Gu, Y. Xia, Z. Wang, X. Liu, J. Xia, S. Zuo, Y. Hu, X. Gao, W. Hui, L. Chao, T. Niu, M. Fang, H. Lu, H. Dong, H. Yu, S. Chen, X. Ran, L. Song, B. Li, J. Zhang, Y. Peng, G. Shao, J. Wang, Y. Chen, G. Xing and W. Huang, *Nat. Energy*, 2021, **6**, 38.
17 L. Mao, Y. Wu, C. C. Stoumpos, M. R. Wasielewski and M. G. Kanatzidis, *J. Am. Chem. Soc.*, 2017, **139**, 5210.
18 D. B. Mitzi, K. Chondroudis and C. R. Kagan, *IBM J. Res. Dev.*, 2001, **45**, 29.
19 M. Seitz, A. J. Magdaleno, N. A. Cano, M. Melendez, T. J. Lubbers, S. W. Walraven, S. Pakdel, E. Prada, R. D.-Buscalioni and F. Prins, *Nat. Commun.*, 2020, **11**, 2035.
20 A. O. E.-Ballouli, O. M. Bakr and O. F. Mohammed, *J. Phys. Chem. Lett.*, 2020, **11**, 5705.
21 M. Wang, J. Tang, H. Wang, C. Zhang, Y. S. Zhao and J. Yao, *Adv. Opt. Mater.*, 2020, **8**, 1901780.
22 P. K. Roy, R. K. Ulaganathan, C. M. Raghavan, S. M. Mhatre, H. I. Lin, W. L. Chen, Y. M. Chang, A. Rozhin, Y. T. Hsu, Y. F. Chen, R. Sankar, F. C. Chou and C. T. Liang, *Nanoscale*, 2020, **12**, 18269.
23 Y. Zhang, Y. Liu, Z. Xu, H. Ye, Q. Li, M. Hu, Z. Yang and S. Liu, *J. Mater. Chem. C*, 2019, **7**, 1584.
24 T. Li, W. A. D. Shohl, E. W. Reinheimer, P. L. Magueres and D. B. Mitzi, *Chem. Sci.*, 2019, **10**, 1168.
25 T. Li, W. A. D. Shohl, Q. Han and D. B. Mitzi, *Chem. Mater.*, 2017, **29**, 6200.
26 E. S. Vasileiadou, I. Hadar, M. Kepenekian, J. Even, Q. Tu, C. D. Malliakas, D. Friedrich, I. Spanopoulos, J. M. Hoffman, V. P. Dravid and M. G. Kanatzidis, *Chem. Mater.*, 2021, **33**, 5085.
27 G. P. Nagabhushana, R. Shivaramaiah and A. Navrotsky, *Proc. Natl. Acad. Sci. U. S. A.*, 2016, **113**, 7717.
28 J. Yang, W. Kang, Z. Liu, M. Pi, L. B. Luo and C. Li, *J. Phys. Chem. Lett.*, 2020, **11**, 6880.
29 M. Shoaib, X. Zhang, X. Wang, H. Zhou, T. Xu, X. Wang, X. Hu, H. Liu, X. Fan, W. Zheng, T. Yang, S. Yang, Q. Zhang, X. Zhu, L. Sun and A. Pan, *J. Am. Chem. Soc.*, 2017, **139**, 15592.
30 J. Yao and G. Yang, *Nanoscale*, 2020, **12**, 454.
31 O. L.-Sanchez, D. Lembke, M. Kayci, A. Radenovic and A. Kis, *Nat. Nanotechnol.*, 2013, **8**, 497.
32 S. Lim, M. Ha, Y. Lee and H. Ko, *Adv. Opt. Mater.*, 2018, **6**, 1800615.
33 F.-X. Liang, J.-J. Jiang, Y.-Z. Zhao, Z.-X. Zhang, D. Wu, L.-H. Zeng, Y. H. Tsang and L.-B. Luo, *Adv. Funct. Mater.*, 2020, **30**, 2001033.
34 J. Zhou, Y. Chu and J. Huang, *ACS Appl. Mater. Interfaces*, 2016, **8**, 25660.
35 R. Dong, C. Lan, X. Xu, X. Liang, X. Hu, D. Li, Z. Zhou, L. Shu, S. Yip, C. Li, S.-W. Tsang and J. C. Ho, *ACS Appl. Mater. Interfaces*, 2018, **10**, 19019.
36 R. Dong, C. Lan, F. Li, S. Yip and J. C. Ho, *Nanoscale Horiz.*, 2019, **4**, 1342.
37 W. Deng, L. Huang, X. Xu, X. Zhang, X. Jin and S.-T. Lee, *Nano Lett.*, 2017, **17**, 2482.
38 Z. Lian, Q. Yan, Q. Lv, Y. Wang, L. Liu, L. Zhang, S. Pan, Q. Li, L. Wang and J.-L. Sun, *Sci. Rep.*, 2015, **5**, 16563.
39 M. Buscema, J. O. Island, D. J. Groenendijk, S. I. Blanter, G. A. Steele, H. S. J. van ser Zant and A. C. Gomez, *Chem. Soc. Rev.*, 2015, **44**, 3691.
40 G. Su, V. G. Hadjiev, P. E. Loya, J. Zhang, S. Lei, S. Maharjan, P. Dong, P. M. Ajayan, J. Lou and H. Peng, *Nano Lett.*, 2015, **15**, 506.
41 N. Huo and G. Konstantatos, *Nat. Commun.*, 2017, **8**, 572.
42 J. Kwon, Y. Shin, H. Kwon, J. Y. Lee, H. Park, K. Watanabe, T. Taniguchi, J. Kim, C. H. Lee, S. Im and G. H. Lee, *Sci. Rep.*, 2019, **9**, 10354.
43 Z. Tan, Y. Wu, H. Hong, J. Yin, J. Zhang, L. Lin, M. Wang, X. Sun, L. Sun, Y. Huang, K. Liu, Z. Liu and H. Peng, *J. Am. Chem. Soc.*, 2016, **138**, 16612.
44 R. K. Ulaganathan, R. C. Murugesan, C. Y. Lin, A. Subramanian, W. L. Chen, Y. M. Chang, A. Rozhin and R. Sankar, *Adv. Funct. Mater.*, 2022, **32**, 2112277.
45 C. M. Raghavan, T. P. Chen, S. S. Li, W. L. Chen, C. Y. Lo, Y. M. Liao, G. Haider, C. C. Lin, C. C. Chen, R. Sankar, Y. M. Chang, F. G. Chou and C. W. Chen, *Nano Lett.*, 2018, **18**, 3221.